2026 IEEE International Conference on Robotics and Automation (ICRA 2026)
June 1-5, 2026. Vienna, Austria

VEGA: A Geometry-Aware Enveloping Layer-based Path Planning Strategy for Accurate Robotic 3D Printing

Won Bin Choi[1] and Wan Kyun Chung[1]

***Abstract*— Additive manufacturing offers extensive design freedom but remains limited by path planning strategies that rely on planar slicing, which introduce staircase artifacts. Non-planar slicing improves local fidelity yet still produces stacking artifacts due to exposed layer boundaries, leaving a gap in capturing complex geometries. This work proposes a Volumetric Envelope Generation Algorithm (VEGA) that generates geometry-aware enveloping layers through a buffering-erosion process. By introducing a Buffer Restraint Region (BRR), the method enables control over incorporation mode and layer positioning. Printability-based splitting further ensures feasible print paths for fabrication. Experiments were conducted on planar- and non-planar-base geometries, printed with a custom 3D printing robot. Printed models were scanned during evaluation, showing reductions of 68.5% in volumetric error, 69.1% in surface deviation, and 77.9% in chamfer distance relative to planar slicing, achieved without additional computational cost (≈32 s per model) or print length. These results demonstrate that enveloping-based path planning effectively mitigates artifacts inherent to slicing-based approaches, providing a strategy for high-fidelity, reliable fabrication of complex geometries.**

I. Introduction

Additive manufacturing (AM) has become a critical fabrication strategy by offering extensive geometric freedom, thereby expanding viable designs in diverse industrial and research applications [1], [2], [3]. In contrast, subtractive processes such as CNC machining achieve high shape fidelity but are constrained by tool accessibility and collision, which limit the range of manufacturable morphologies [4], [5]. AM overcomes these restrictions by depositing material layer by layer, enabling fabrication of geometries inaccessible to subtractive processes, including intricate or internal shapes common in biomedical, aerospace, and architectural applications [2], [6], [7], [8], [9].

Notably, extrusion-based printing has become one of the most widely adopted AM processes due to its versatility and ease of implementation [1], [10], [11], [12]. Despite this wide adoption, most extrusion-based print systems still rely on planar deposition strategies that restrain accurate reproduction of non-planar features such as inclines or curves, resulting in deviations between the printed and target geometries (e.g., staircase artifact) (Fig. 1) [2], [7], [13], [14]. As a result, such inaccuracies can compromise the functional integrity of the part and hinder its design purpose. This limitation can be compensated by constraining or modifying the original design, but this undermines the geometric freedom of AM. Alternatively, higher print resolutions or post-processing can be used, but these prolong fabrication time and become impractical for time-critical applications (e.g., bioprinting, thermal-stress-limited processes) [1], [15]. Therefore, addressing these geometric mismatches requires toolpaths that utilize the full spatial degrees of freedom rather than being restricted to planar layers. In this context, robotic, multi-axis AM provides complete control of tool position and orientation to print along geometry-aware paths, enabling faithful replication of complex geometries.

In robotic AM, depositing material along true 3D fabrication paths requires path planning strategies that account

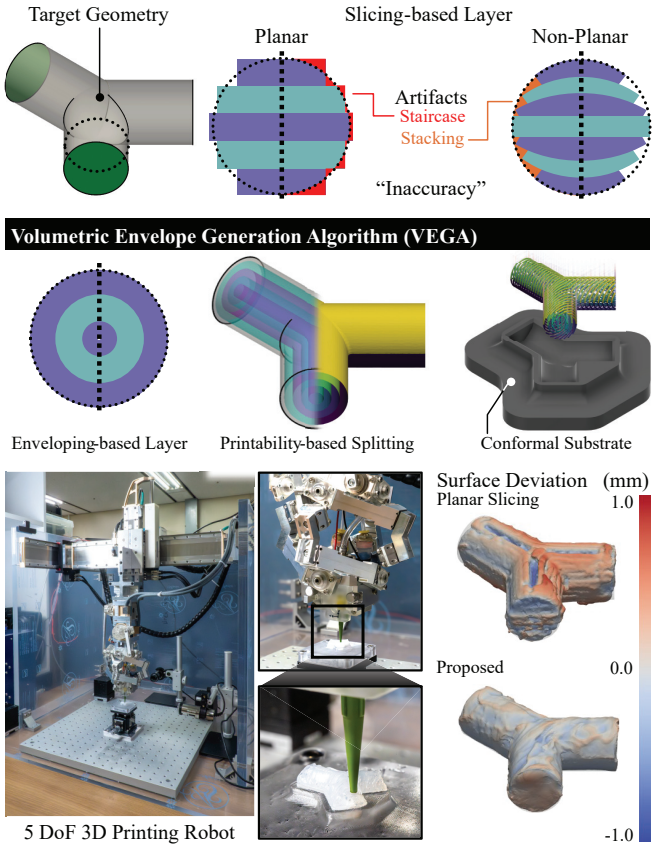

Fig. 1. Overview of the Volumetric Envelope Generation Algorithm (VEGA). Conventional slicing introduces artifacts in non-planar geometries. This is addressed by generating geometry-aware enveloping layers through a buffering-erosion process, and validation with a custom 5 DoF 3D printing robot demonstrated enhanced shape fidelity.

*This work was supported by the Alchemist Project 2410012609 (20012378, Development of Meta Soft Organ Module Manufacturing Technology without Immunity Rejection and Module Assembly Robot System) funded By the Ministry of Trade, Industry & Energy (MOTIE, Korea).

[1] The authors are with the Department of Mechanical Engineering, Pohang University of Science and Technology, Pohang 37673, Republic of Korea. wkchung@postech.ac.kr

for the 3D morphology of the target geometry, in contrast to conventional planar printing that layers 2D slices. Non-planar slicing methods address this requirement by generating fabrication trajectories from approaches such as objective-based optimization [16], [17], field-based layer construction [18], [19], [20], [21], and computational geometry [22], [23], [24] to produce non-planar layers. However, while non-planar slicing enhances local fidelity on non-planar features, it remains prone to 'stacking artifacts' (Fig. 1). Depending on how the layers are stacked, layer boundaries may be exposed on the surface, where their accumulation forms defects, resulting in inaccuracies. This reveals a gap in non-planar path planning: the need for an algorithmic strategy that can generate geometry-aware non-planar layers while also controlling their mode of incorporation and positioning within the target geometry. Such a strategy enables the mitigation of artifacts inherent to slicing algorithms, thereby enabling accurate reproduction of complex geometries.

Since stacking artifacts arise from exposed layer boundaries in conventional slicing algorithms, their influence can be reduced by embedding these boundaries within the volume. So, instead of simply stacking non-planar slices, layers can be generated as target geometry-based envelopes that incorporate the stacks within the volume to mitigate stacking effects. Therefore, we developed an algorithmic pipeline that generates shape-reflective layers with the capability to concurrently tune their enveloping properties to control incorporation mode and stack positioning. With this layer generation approach, robotic AM mitigates staircase and stacking artifacts, enabling accurate fabrication of complex geometries.

We propose a layer generation strategy that creates geometry-aware enveloping layers with the capability to control their incorporation mode and positioning within the volume (Fig. 1). This enveloping scheme eliminates artifacts inherently generated by conventional slicing approaches—namely staircase and stacking artifacts—leading to enhanced accuracy in non-planar 3D printing. To realize this scheme, the algorithm constructs layers through an iterative buffering-erosion process. Given a surface mesh as input, the process begins by buffering the target geometry shell with a constant inward and outward offset equal to the user-defined layer thickness. This offsetting is implemented through a Minkowski sum with a spherical structuring element. A set difference operation between the buffered surface and target geometry then produces an eroded geometry, which serves as the input for the next iteration; repeating this process until the volume is fully diminished yields a sequence of eroded geometries that collectively serve as enveloping layers representing the target geometry. The buffering can be selectively modified by defining regions where no buffer is applied, thereby altering the buffer volume and the resulting eroded geometry that acts as the layer. This, in turn, governs the incorporation mode of the envelopes, providing control over how the layers embed within the geometry. In this way, geometry-aware '**enveloping**' layers are generated that capture the complexity of the target shape while mitigating artifacts of conventional '**slicing**'-based algorithms. We validated this approach by printing selected models with different path-planning algorithms, scanning the results with a 3D scanner, and evaluating dimensional accuracy with multiple shape-fidelity metrics. The main contributions of this work are:

- An algorithmic pipeline that generates print paths from geometry-aware enveloping layers via buffering-erosion process with controllable incorporation mode, mitigating geometric artifacts common to conventional slicing-based algorithms.
- A technique for controlling the incorporation mode of enveloping layers by applying constraints on the buffering process, enabling adjustable layer embedding within the geometry.
- A printability filter to assess enveloping layers, with a printability-based splitting strategy that divides layers into sublayers to ensure printability.

The rest of this article is structured as follows. Section II introduces the detailed approach of the proposed algorithm. Section III details the experimental setup and evaluation methodology. Section IV reports the findings and presents a quantitative assessment. Section V summarizes the study and identifies directions for future research.

II. Methods

Let A_{-1} denote the reference geometry corresponding of the solid intended to print.

1) **Initial Surface Extraction.** The process begins by taking the target geometry surface ($\partial A_i = \{\boldsymbol{a} | \boldsymbol{a} \in \partial A_i\}$) from the reference geometry (Fig. 2(a)).
2) **Minkowski Sum.** A Minkowski sum is applied between the surface and a structuring element solid, ($B = \{\boldsymbol{b} | \boldsymbol{b} \in B\}$) (Fig. 2(b)), yielding the buffered geometry solid

$$C = \partial A_i \oplus B$$

The operation ($\partial A_i \oplus B$) offsets the surface (∂A_i) in both inward and outward directions (Fig. 2(c)) using a structuring element.

In our method, the structuring element for the Minkowski sum is defined as a sphere, ensuring that the buffered geometry maintains a constant surface offset while preserving the morphology of the target geometry. For the initial layer, the sphere radius is set to half of the layer thickness; for all subsequent layers, the radius equals the layer thickness.

3) **Erosion via Set Difference.** A set difference is then computed between the target geometry and the buffered solid:

$$D = A_i \backslash C$$

The result is an eroded geometry solid (D) that captures the interior surface offset morphology (Fig. 2(d)).

4) **Iterative Layer Generation.** The eroded geometry surface (∂D) is assigned as the $(i+1)^{th}$ print layer,

$$\partial A_{i+1} = \partial D$$

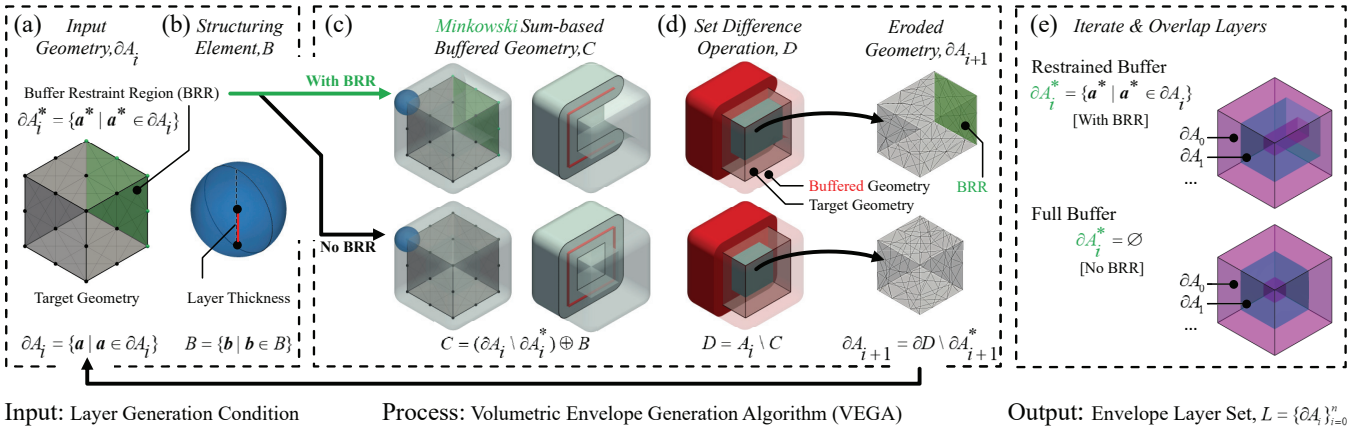

Fig. 2. Process of generating enveloping layers through an iterative buffering-erosion procedure of VEGA. (a) Layer generation conditions are defined by setting the Buffer Restraint Region (BRR) on the target geometry. (b) A spherical structuring element is chosen for constant offsetting. (c) Applying the Minkowski sum yields the buffered geometry, and a (d) set-difference operation produces the eroded geometry. (e) Iterating this process until the eroded volume diminishes produces a sequence of eroded geometries, which are collected to form the envelope layer set.

which also serves as the input for the subsequent buffering–erosion iteration (Steps 2 to 4).

The buffering–erosion process is iterated until the eroded geometry volume diminishes to zero. Collecting the resulting layers yields an envelope layer set ($L = \{\partial A_i\}_{i=0}^n$), where each surface ∂A_i represents an enveloping layer making up the reference geometry (A_{-1}) (Fig. 2(e)). We propose this process as the Volumetric Envelope Generation Algorithm (VEGA), which constitutes the core mechanism of our method.

The buffering-erosion process generates a sequence of layers that resemble the reference geometry (A_{-1}). These layers propagate in a concentric manner and ultimately form completely enclosed shells around the geometry. We refer to this type of layer generation as the 'full' buffering-erosion process. While this representation accurately preserves the geometry, the resulting enclosed shells introduce printing challenges. In particular, path generation becomes challenging because enclosed shells create risks of collision, especially near the print base. Moreover, printing such shells requires resolving the order of deposition—inside-out or outside-in—yet certain regions remain impossible to print without collision. Finally, completely enclosed layers demand that the printing robot possess a large reachable workspace for collision avoidance, even when fabricating relatively small models, due to manipulability constraints. To address these difficulties, the strategy must adapt to the characteristics of the reference geometry. Two distinct cases can be considered: 1) geometry with planar features, 2) geometry with high non-planarity.

In the first case, where the **geometry contains planar features**, the enveloping behavior of VEGA can be relaxed from full enclosure to regional enveloping. This adjustment allows stacking artifacts to be intentionally positioned on planar regions, where their influence on accuracy can be suppressed and overall printability is improved.

A Buffer Restraint Region (BRR) is defined as

$$\partial A_i^* = \{\boldsymbol{a}^* | \boldsymbol{a}^* \in \partial A_i\}$$

which is a subsurface of the target geometry surface ($\partial A_i^* \subseteq \partial A_i$) that can be directly selected by the user (Fig. 2(a)). By introducing the BRR, this region is excluded from the buffering operation in the Minkowski sum, thereby producing a restrained buffered solid

$$C = (\partial A_i \backslash \partial A_i^*) \oplus B$$

Since erosion is derived from the buffered solid, any change in buffering propagates to the erosion step (Fig. 2(c), (d)). Accordingly, the layer assignment is redefined by excluding the next BRR (∂A_{i+1}^*) from the eroded geometry

$$\partial A_{i+1} = \partial D \backslash \partial A_{i+1}^*$$

The remainder of the procedure is equivalent to the full buffering-erosion process, with the distinction summarized as follows (Fig. 2(e)):

1) Full buffering-erosion process: $\partial A_i^* = \varnothing$
2) Restrained buffering-erosion process: $\partial A_i^* = \{\boldsymbol{a}^* \mid \boldsymbol{a}^* \in \partial A_i\}$

In summary, the user's definition of the BRR modifies the buffered geometry morphology, which subsequently determines the morphology of the generated layers. After the layers are collected into the envelope layer set, their propagation and enveloping behavior are governed by the BRR, which controls the incorporation mode, positioning, and structure of the layers. This enables intentional guidance of stack artifact placement, allowing their influence to be mitigated according to the geometry of the target model.

While the BRR provides local control over layer morphology, enabling volumetric layer generation further requires that the BRR be transferred across successive layers. After the initial manual selection, this transfer eliminates the need for repeated user input. The main challenge is that the next layer (∂A_{i+1}) may contain multiple subsurface candidates

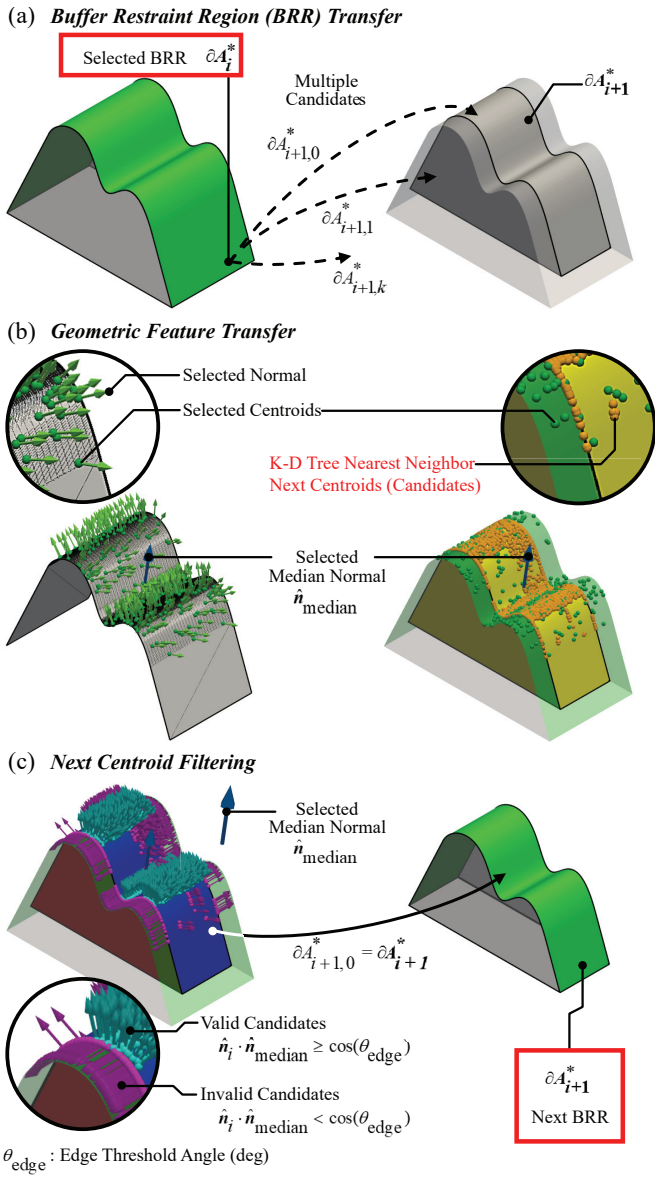

Fig. 3. BRR transfer method for the restrained buffering–erosion process in VEGA. (a) The initial BRR is manually defined, but subsequent layers yield multiple candidates. (b) Candidate centroids are identified using geometric feature extraction and K-D tree search. (c) The next BRR is selected by filtering candidate normals against the selected median normal of the previous BRR.

($\partial A_{i+1,k}^*$), requiring a method to identify the one most consistent with the previously selected BRR (Fig. 3(a)).

The transfer process begins with geometric feature transfer, which extracts the subsurface corresponding to the chosen BRR, computes centroids and surface normals from its triangular mesh, and derives a representative selected median normal ($\hat{\boldsymbol{n}}_{\text{median}}$) (Fig. 3(b)). This median normal is obtained using the spherical L1 formulation,

$$\hat{\boldsymbol{n}}_{\text{median}} = \arg\min_{\hat{\boldsymbol{n}} \in S^2} \sum_{i=1}^{N} \arccos\left(\hat{\boldsymbol{n}} \cdot \hat{\boldsymbol{n}}_i\right)$$

which yields a robust representative direction, as it is less sensitive to outliers. The centroids are then used to query nearest neighbors in the next layer centroids via a K-D Tree, producing an initial candidate set.

These candidates are filtered by comparing their local surface normals with the selected median normal ($\hat{\boldsymbol{n}}_{\text{median}}$) using cosine similarity (Fig. 3(c)). The edge threshold angle (θ_{edge}) defines the maximum allowable deviation between normals, distinguishing whether neighboring triangles belong to the same surface or represent distinct ones. Therefore, centroids that satisfy $\hat{\boldsymbol{n}}_i \cdot \hat{\boldsymbol{n}}_{\text{median}} \geq \cos(\theta_{\text{edge}})$ are retained as valid candidates, where one is randomly selected to define the next BRR.

In the second case, where the **geometry exhibits high non-planarity** and lacks planar features, the concentric enclosing layers must be maintained. As previously noted, enclosed shell layers generated by 'full' buffering-erosion process present significant printing challenges, including collision risks, deposition order conflicts, and high workspace requirements. For such situations, a layer topology transition method is introduced, in which the layer is split according to printability to adjust its topology.

To evaluate the printability of each enveloping layer, we take a layer surface ∂A_i and apply two filters: orientation reachability and tool accessibility.

The orientation reachability filter (f_1) checks whether the robot can reach the surface of the i^{th} layer. This is performed through an inverse kinematic analysis, and if a joint configuration q exists within the valid joint space Q_{valid}, then the layer surface is considered reachable and $f_1 = \text{True}$.

The tool accessibility filter (f_2) evaluates whether the nozzle can approach the target surface without collision. We define the longitudinal tool axis as $\hat{z}_{\text{tool}}$, pointing toward the nozzle tip, and the target position on the surface as p_{tool}. The nozzle approaches along $\hat{z}_{\text{tool}}$, which does not need to coincide with the surface normal, but instead follows the orientation design policy selected by the user. In our study, we set $\hat{z}_{\text{tool}}$ to match the surface normal. Accessibility is then determined by verifying whether the approach line

$$l(\lambda) = p_{\text{tool}} + \lambda \hat{z}_{\text{tool}}, \quad \lambda > 0$$

intersects the surface ∂A_i only at the target position (p_{tool}). If this condition holds, then $f_2 = \text{True}$.

Printability of the layer is determined by applying the logical operator $F_p[\partial A_i] = f_1[\partial A_i] \wedge f_1[\partial A_i]$ (Fig. 4(a)). If all regions of every layer in the envelope layer set (L) satisfy the printability condition, the set is classified as *Fully Printable* (Fig. 4(a) - Left). In this case, it is passed to the layer sorting process.

If one or more regions of the surface fail the printability check, the layer is marked unprintable (Fig. 4(a) - Right). To resolve this, we first distinguish and extract the printable and unprintable regions from the results of the printability analysis. The boundary points between these regions are extracted, and a separating surface is reconstructed using Gaussian Process regression with an RBF kernel, which also provides uncertainty estimation for noisy boundaries.

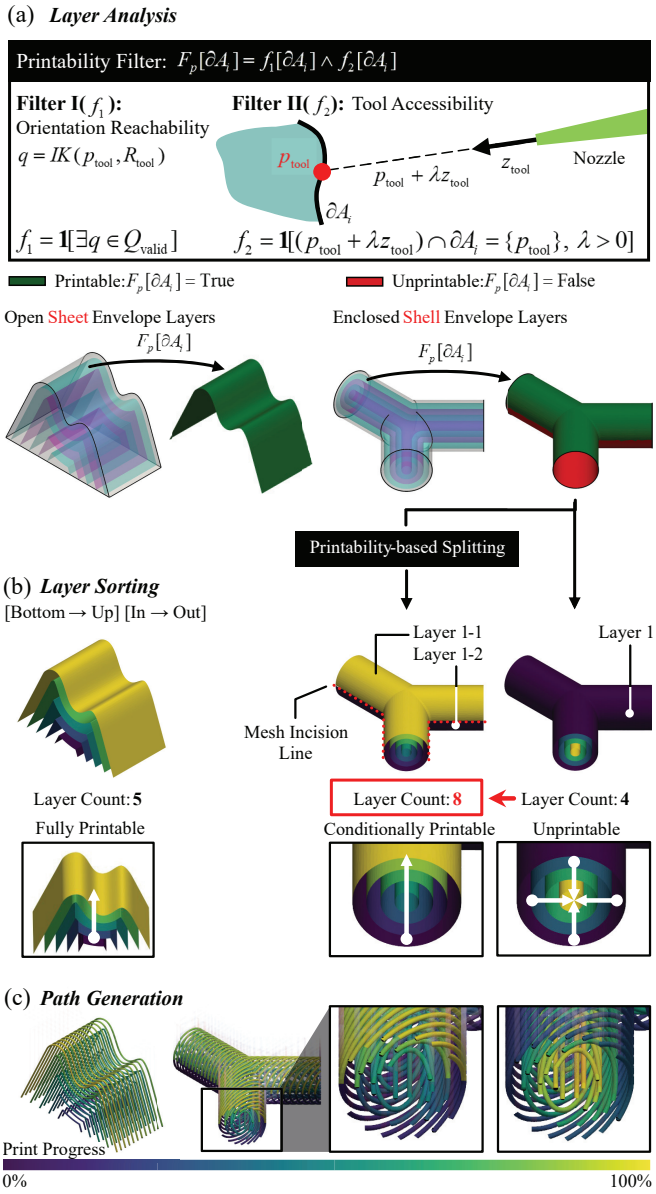

Fig. 4. Layer decomposition method for geometries with high non-planarity. (a) Printability analysis using orientation reachability and tool accessibility filters. (b) Fully printable layers proceed directly, while unprintable enclosed layers are split along printability boundaries to enable conditional printability and avoid collisions. (c) Verified layers are ordered and print paths are generated by projecting user-defined patterns.

Using the reconstructed separation surface, the unprintable enclosed shell layer is split into multiple open layers, which are then processed by the layer sorting procedure. Through this mechanism, originally unprintable enclosed shells can be made *conditionally printable*. This resolves the problem of enclosed shell layers either blocking access to the inner region or colliding with pre-printed layers (Fig. 4(b)).

After verification and splitting, the layers are sorted from bottom to top, and within the same level, from inside to outside. Path generation is then applied to the ordered layers, where tool paths are generated according to user-defined parameters such as interval distance, orientation, and pattern (Fig. 4(c)). Print paths are computed by first generating a line pattern from these parameters and subsequently projecting it onto the layer surfaces.

In summary, the algorithm takes a target model as input and generates print paths through the proposed pipeline. The process begins with layer generation through VEGA, which produces an envelope layer set. Users can control the enveloping behavior by defining a BRR, thereby selecting either a restrained or full buffer-erosion process depending on the application. The generated layers are then subjected to printability analysis, where unprintable regions are modified through printability-based splitting to achieve conditional printability. Finally, the verified layers are ordered, and tool paths are generated according to user-defined parameters.

III. Experiment

Experiments were conducted to evaluate whether the proposed non-planar path planning algorithm improves reproduction accuracy for geometries with complex non-planar features. To this end, we compared two algorithms: the conventional planar slicing algorithm, which uses concentric infill patterns, and our proposed method. Two categories of geometries were tested, one with planar bases and the other with non-planar bases, each consisting of three shapes, for a total of six geometries (Fig. 5(a)). For each geometry, print paths were generated using both algorithms, and the resulting parts were fabricated with our custom multi-axis 3D printing robot for direct comparison against the target models.

We used a custom-built 5 DoF 3D printing robot consisting of a pneumatic gravity compensator to minimize gravitational effects (Fig. 5(b)). The robot is equipped with a direct ink writing (DIW) tool head, driven by a pneumatic dispenser (S-SIGMA-CM3-V2; Musashi Engineering, Inc., Japan) for precise material extrusion.

Real-time multi-axis motion control is achieved via EtherCAT, which drives high-precision actuators (LINAX Lxs 400/160 F60, ROTAX Rxhq 50; Jenny Science, Switzerland) through a motor driver (Xvi 75v8-EtherCAT; Jenny Science, Switzerland), enabling custom controller implementation. A disturbance-compensated PID controller was employed using force-sensing data from a calibration process to achieve disturbance rejection. Trajectory tracking tests demonstrated a mean absolute error (MAE) of 9.4 ± 1.08 μm with a repeatability of ± 2 μm, confirming precise and accurate motion characteristics.

The experiments were conducted using a silicone polymer-based material (SE 1700; DOWSIL, USA), loaded into the DIW print head equipped with a tapered 18G nozzle (TPND-18G-U; Musashi Engineering, Japan) having an inner diameter of 0.84 mm. Printing was performed at a pneumatic extrusion pressure of 130 kPa and a speed of 5 mm/s, using an envelope layer thickness of 0.80 mm (Fig. 5(b)). This produced print lines with an average width of 1.2 mm. The prints were performed on a platform with conformal (geometry-matched) substrates shaped to match the non-planar bases of the target geometries. After printing, the

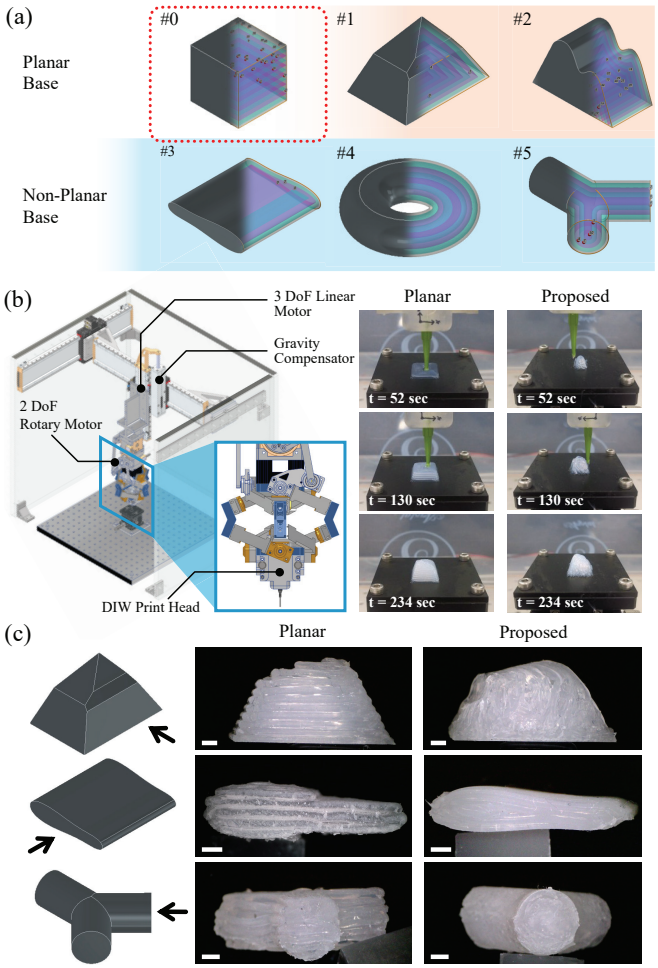

Fig. 5. Experimental validation of the proposed non-planar path-planning algorithm. (a) Six test geometries with planar- and non-planar-base groups. (b) Custom multi-axis 3D printing robot used for fabrication. (c) Printed results for comparison (Scale bar = 2 mm).

parts were thermally cured at 60 °C for 12 h to complete crosslinking of the silicone polymer-based material.

Post-print evaluation began with visual inspection of the fabricated models, where placing the prints side by side revealed structural artifacts such as staircase and stacking effects in the printed models. For a stricter evaluation, we used a 3D scanner (CR-Scan Raptor; Creality, China) to obtain the external profiles of the printed models and analyze the print fidelity of both the planar slicing and the proposed algorithm. The scanning process produced surface mesh data, which was then compared against the target model A_{-1}, hereafter referred to as the ground truth mesh A_{GT}. To enable accurate comparison, the scanned mesh was first coarsely aligned to the reference using scan maker-based manual overlap, followed by refinement through ICP (Iterative Closest Point) registration.

After mesh alignment, the accuracy of the printed models was evaluated using three metrics that quantify shape fidelity:

1) **Volumetric Error** (e_1)

$$e_1 = \frac{V_{\text{under}} + V_{\text{over}}}{V_{\text{GT}}} \times 100(\%)$$

where V_{under} and V_{over} represent the under- and over-shoot volumes of the scanned mesh relative to the ground truth volume V_{GT}. This metric measures the ratio of misprinted volume to the ground truth, with $e_1 \to 0.0$ indicating higher accuracy.

2) **Surface Deviation** (e_2)

$$e_2 = \phi(x)\big|_{x\in\partial A_{\text{scan}}} = \begin{cases} -\inf\limits_{y\in\partial A_{\text{GT}}} \|x-y\|, & x \in A_{\text{GT}}, \\ 0, & x \in \partial A_{\text{GT}}, \\ \inf\limits_{y\in\partial A_{\text{GT}}} \|x-y\|, & x \notin A_{\text{GT}}. \end{cases}$$

Here, $\phi(x)$ denotes the signed distance function with respect to the ground truth surface ∂A_{GT}. Negative values indicate points inside the ground truth, positive values indicate points outside, and zero corresponds to perfect alignment. Thus, $e_2 \to 0.0$ reflects increasing geometric accuracy.

3) **Chamfer Distance** (e_3)

$$e_3 = \frac{1}{|P_{\text{s}}|}\sum_{x\in P_{\text{s}}} \min_{y\in P_{\text{GT}}} \|x-y\|^2 + \frac{1}{|P_{\text{GT}}|}\sum_{y\in P_{\text{GT}}} \min_{x\in P_{\text{s}}} \|x-y\|^2$$

Here, P_{s} and P_{GT} denote the point clouds of the scanned and ground truth meshes, respectively, corresponding to their vertices in our case. This metric computes the average squared nearest-neighbor distance between the two point sets, with $e_3 \to 0.0$ indicating closer alignment.

Together, these three metrics capture volumetric, surface-level, and point-level fidelity, providing a comprehensive evaluation of print accuracy.

Among the six models, five (#1 - #5) were evaluated through 3D scanning, while model #0 was printed separately to demonstrate that the proposed algorithm can also generate planar layers equivalent to conventional slicing. These experiments provide the basis for the quantitative and qualitative evaluations presented in the following section.

IV. Results

This section presents results comparing the proposed algorithm with conventional planar slicing, using both qualitative observations and quantitative metrics of print fidelity.

Compared to conventional slicing-based approach, where staircase and stacking artifacts were commonly observed, prints generated using the proposed algorithm exhibited geometric profiles with minimal artifacts, successfully capturing non-planar features such as inclines and curves (Fig. 5(c))

In addition to print fidelity, the computational performance of the algorithm was assessed. Across 30 trials with varied geometries and print parameters, the average computation time was 32 ±7 sec, measured from algorithm initiation to final trajectory data output, excluding manual selection of the BRR.

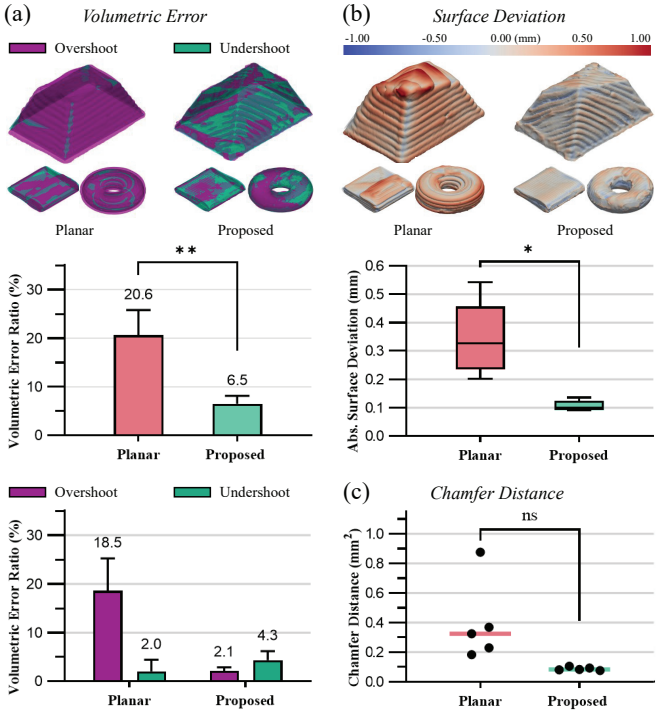

Fig. 6. Quantitative evaluation of print fidelity between the proposed algorithm and conventional planar slicing. Metrics include (a) volumetric error, (b) surface deviation, and (c) chamfer distance. Across all measures, the proposed algorithm produced prints with substantially higher geometric accuracy.

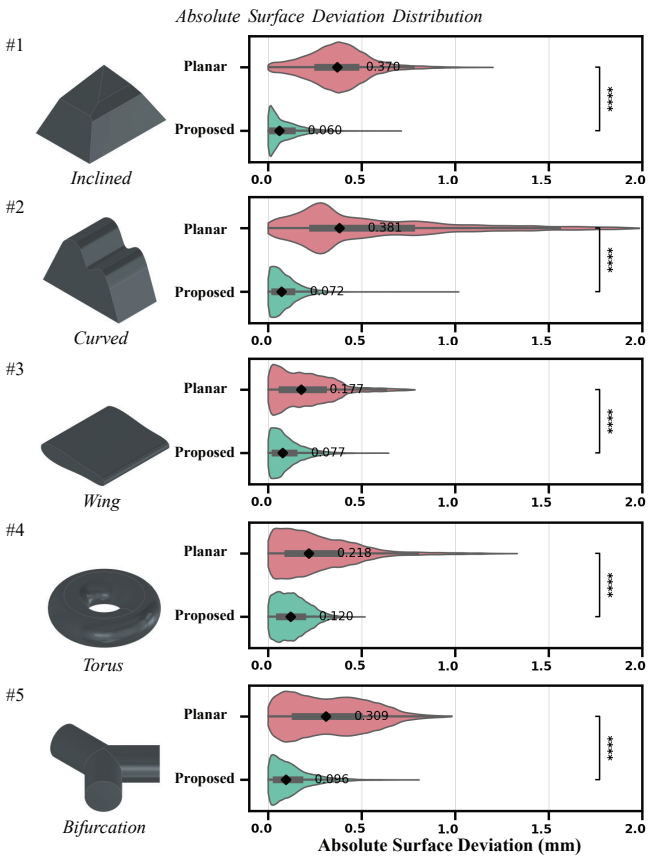

Fig. 7. Distribution of absolute surface deviation across tested geometries, visualized with violin plots. The proposed algorithm exhibits distributions concentrated closer to 0.0 across all tested geometries, indicating higher print accuracy compared to planar slicing.

Beginning with the volumetric error, the proposed algorithm significantly reduced the error by 68.5% compared to planar slicing (Fig. 6(a)). Decomposing the volumetric error into overshoot and undershoot components revealed that the overshoot ratio was reduced by 88.5%, while the undershoot ratio increased by 113.7%. The undershoot increase stemmed from using Euclidean line spacing in path generation, which creates larger gaps on highly non-planar regions (Fig. 4(c)); this could be mitigated by adopting geodesic spacing.

In surface deviation, the deviation distribution was visualized using heatmaps of selected scanned models, indicating where geometric errors occurred (Fig. 6(b)). For statistical analysis, the absolute surface deviation was measured, showing that planar slicing produced a deviation of 0.342 ± 0.129 mm, whereas the proposed algorithm achieved 0.106 ± 0.019 mm. This corresponds to a 69.1% reduction in surface deviation. A violin plot was generated for each test geometry to visualize the distribution of absolute surface deviation. Overall, the proposed algorithm produced distributions concentrated closer to 0.0, indicating higher surface fidelity compared to planar slicing (Fig. 7).

Finally, the chamfer distance was evaluated to assess point-level alignment between the scanned and ground truth geometries (Fig. 6(c)). The proposed algorithm showed a 77.9% decrease in chamfer distance compared to planar slicing, although the difference was not statistically significant. Even so, the distribution for the proposed algorithm (0.088 ± 0.012) was much narrower than that of planar slicing (0.397 ± 0.297), indicating greater consistency in point-level accuracy.

Print time was calculated by dividing the total path length by a constant end-effector linear speed. Across all six geometries, the proposed algorithm differed by $5.4 \pm 2.3\%$ (n=30) from planar slicing, indicating no excessive increase in print time.

V. Conclusion

This work presents a non-planar path-planning algorithm for robotic 3D printing that generates and controls enveloping layers to enable accurate fabrication of target geometries with non-planar features. The algorithm employs a buffering-erosion process to produce layers that reflect the target morphology, while allowing the user to adjust the enveloping action to control layer propagation for internal structure control and mitigate artifacts commonly observed in conventional slicing.

The current implementation requires a conformal substrate to be fabricated prior to the printing process. The generation of this additional support structure can be automated using support generation methods similar to those introduced in previous work [25]. In future work, we plan to integrate this support generation process into the system to further

streamline the fabrication of non-planar geometries.

By reformulating path planning as an *enveloping process*, the method achieves high-fidelity reproduction of non-planar geometries while reducing artifacts inherent to conventional slicing, establishing a foundation for accurate, reliable, and versatile fabrication of complex geometries.

REFERENCES

[1] S. C. Altıparmak, V. A. Yardley, Z. Shi, and J. Lin, "Extrusion-based additive manufacturing technologies: State of the art and future perspectives," *Journal of Manufacturing Processes*, vol. 83, pp. 607–636, 2022.

[2] P. Tang, X. Zhao, H. Shi, B. Hu, J. Ding, B. Yang, and W. Xu, "A review of multi-axis additive manufacturing: Potential, opportunity and challenge," *Additive Manufacturing*, vol. 83, p. 104075, mar 2024. [Online]. Available: https://linkinghub.elsevier.com/retrieve/pii/S2214860424001210

[3] Y. Yao, L. Cheng, and Z. Li, "A comparative review of multi-axis 3d printing," *Journal of Manufacturing Processes*, vol. 120, pp. 1002–1022, 2024. [Online]. Available: https://www.sciencedirect.com/science/article/pii/S1526612524004432

[4] Z. Zhang, J. Yan, and T. Kuriyagawa, "Manufacturing technologies toward extreme precision," *International Journal of Extreme Manufacturing*, vol. 1, no. 2, p. 22001, 2019. [Online]. Available: http://dx.doi.org/10.1088/2631-7990/ab1ff1

[5] I. Gibson, D. Rosen, B. Stucker, M. Khorasani, D. Rosen, B. Stucker, and M. Khorasani, *Additive manufacturing technologies*. Springer, 2021, vol. 17.

[6] S. Vanaei, M. S. Parizi, S. Vanaei, F. Salemizadehparizi, and H. R. Vanaei, "An Overview on Materials and Techniques in 3D Bioprinting Toward Biomedical Application," *Engineered Regeneration*, vol. 2, no. November 2020, pp. 1–18, 2021. [Online]. Available: https://doi.org/10.1016/j.engreg.2020.12.001

[7] T. D. Ngo, A. Kashani, G. Imbalzano, K. T. Nguyen, and D. Hui, "Additive manufacturing (3D printing): A review of materials, methods, applications and challenges," *Composites Part B: Engineering*, vol. 143, pp. 172–196, 2018.

[8] I. T. Ozbolat and M. Hospodiuk, "Current advances and future perspectives in extrusion-based bioprinting," *Biomaterials*, vol. 76, pp. 321–343, jan 2016. [Online]. Available: https://linkinghub.elsevier.com/retrieve/pii/S0142961215008868

[9] S. V. Murphy and A. Atala, "3D bioprinting of tissues and organs," *Nature Biotechnology*, vol. 32, no. 8, pp. 773–785, aug 2014. [Online]. Available: https://www.nature.com/articles/nbt.2958

[10] A. I. Nurhudan, S. Supriadi, Y. Whulanza, and A. S. Saragih, "Additive manufacturing of metallic based on extrusion process: A review," *Journal of Manufacturing Processes*, vol. 66, pp. 228–237, 2021.

[11] K. Rane and M. Strano, "A comprehensive review of extrusion-based additive manufacturing processes for rapid production of metallic and ceramic parts," *Advances in Manufacturing*, vol. 7, no. 2, pp. 155–173, 2019.

[12] X. Zhai, L. Jin, and J. Jiang, "A survey of additive manufacturing reviews," *Materials Science in Additive Manufacturing*, vol. 1, no. 4, 2022.

[13] J. S. Chohan, R. Singh, K. S. Boparai, R. Penna, and F. Fraternali, "Dimensional accuracy analysis of coupled fused deposition modeling and vapour smoothing operations for biomedical applications," *Composites Part B: Engineering*, vol. 117, pp. 138–149, 2017.

[14] D. Ahlers, F. Wasserfall, N. Hendrich, and J. Zhang, "3d printing of nonplanar layers for smooth surface generation," in *2019 IEEE 15th International Conference on Automation Science and Engineering (CASE)*, 2019, pp. 1737–1743.

[15] Y. S. Zhang, G. Haghiashtiani, T. Hübscher, D. J. Kelly, J. M. Lee, M. Lutolf, M. C. McAlpine, W. Y. Yeong, M. Zenobi-Wong, and J. Malda, "3D extrusion bioprinting," *Nature Reviews Methods Primers*, vol. 1, no. 1, p. 75, nov 2021. [Online]. Available: https://www.nature.com/articles/s43586-021-00073-8

[16] G. Fang, T. Zhang, S. Zhong, X. Chen, Z. Zhong, and C. C. Wang, "Reinforced FDM: Multi-axis filament alignment with controlled anisotropic strength," *ACM Transactions on Graphics*, vol. 39, no. 6, 2020.

[17] J. Kipping, D. Nettig, and T. Schüppstuhl, "Looping: Load-oriented optimized paths in non-planar geometry," *Additive Manufacturing*, vol. 94, p. 104426, 2024. [Online]. Available: https://www.sciencedirect.com/science/article/pii/S221486042400472X

[18] J. Etienne, N. Ray, D. Panozzo, S. Hornus, C. C. L. Wang, J. Martínez, S. McMains, M. Alexa, B. Wyvill, and S. Lefebvre, "CurviSlicer," *ACM Transactions on Graphics*, vol. 38, no. 4, pp. 1–11, aug 2019. [Online]. Available: https://dl.acm.org/doi/10.1145/3306346.3323022

[19] T. Zhang, G. Fang, Y. Huang, N. Dutta, S. Lefebvre, Z. M. Kilic, and C. C. L. Wang, "S3-slicer: A general slicing framework for multi-axis 3d printing," *ACM Trans. Graph.*, vol. 41, no. 6, Nov. 2022. [Online]. Available: https://doi.org/10.1145/3550454.3555516

[20] Y. Shan, Y. Shui, J. Hua, and H. Mao, "Additive manufacturing of non-planar layers using isothermal surface slicing," *Journal of Manufacturing Processes*, vol. 86, pp. 326–335, 2023. [Online]. Available: https://www.sciencedirect.com/science/article/pii/S1526612522009173

[21] X. Li, W. Liu, Z. Hu, C. He, J. Ding, W. Chen, S. Wang, and W. Dong, "Supportless 3d-printing of non-planar thin-walled structures with the multi-axis screw-extrusion additive manufacturing system," *Materials & Design*, vol. 240, p. 112860, 2024. [Online]. Available: https://www.sciencedirect.com/science/article/pii/S0264127524002338

[22] G. M. Fortunato, M. Nicoletta, E. Batoni, G. Vozzi, and C. De Maria, "A fully automatic non-planar slicing algorithm for the additive manufacturing of complex geometries," *Additive Manufacturing*, vol. 69, no. April, p. 103541, 2023. [Online]. Available: https://doi.org/10.1016/j.addma.2023.103541

[23] M. Danielczuk, A. Angelova, V. Vanhoucke, and K. Goldberg, "X-Ray: Mechanical search for an occluded object by minimizing support of learned occupancy distributions," *IEEE International Conference on Intelligent Robots and Systems*, pp. 9577–9584, 2020.

[24] L. Pelzer and C. Hopmann, "Additive manufacturing of non-planar layers with variable layer height," *Additive Manufacturing*, vol. 37, no. September 2020, p. 101697, 2021. [Online]. Available: https://doi.org/10.1016/j.addma.2020.101697

[25] T. Zhang, Y. Huang, P. Kukulski, N. Dutta, G. Fang, and C. C. Wang, "Support generation for robot-assisted 3d printing with curved layers," in *2023 IEEE International Conference on Robotics and Automation (ICRA)*, 2023, pp. 12 338–12 344.